Numerical Simulation and Experimental Study on the Aerodynamics of Propulsive Wing for a Novel Electric Vertical Take-Off and Landing Aircraft

Junjie Wang [1], **Xinfeng Zhang** [2,*], **Jiaxin Lu** [3] and **Zhengfei Tang** [3]

[1] School of Mechanical Engineering, Jiangsu University of Science and Technology, Zhenjiang 212003, China; wang_junjie@nuaa.edu.cn

[2] School of Information and Electrical Engineering, Hangzhou City University, Hangzhou 310011, China

[3] Academy of Astronautics, Nanjing University of Aeronautics and Astronautics, Nanjing 210016, China; jiaxinlu@nuaa.edu.cn (J.L.); 18167015552@163.com (Z.T.)

[*] Correspondence: zxf@hzcu.edu.cn

Abstract: The electric vertical take-off and landing (eVTOL) aircraft offers the advantages of vertical take-off and landing, environmental cleanliness, and automated control, making it a crucial component of future urban air traffic. As competition intensifies, demands for aircraft performance are escalating, including forward flight speed and payload capacity. The article presents a novel eVTOL design with propulsive wings and establishes methodologies for propulsive wing unsteady numerical simulation and wind tunnel experiments, analyzing its aerodynamic characteristics and lift enhancement mechanism. The results indicate that the cross-flow fan (CFF) provides unique airflow control capabilities, enabling the propulsive wing to achieve remarkably high lift coefficients (exceeding 7.6 in experiments) and propulsion coefficients (exceeding 7.1 in experiments) at extreme angles of attack (30°~40°) and low airspeeds. On the one hand, the CFF effectively controls boundary layer flow, delaying airflow separation at high angles of attack; on the other hand, the rotation of the CFF induces two eccentric vortices, generating vortex-induced lift and propulsion. The aerodynamic performance of the propulsive wing depends on the advance ratio and angle of attack. Typically, both lift and propulsion coefficients increase with the advance ratio, while lift and drag coefficients increase with the angle of attack. The propulsive wing shows significant advantages and prospects for eVTOL aircrafts in the low flight velocity range (0–30 m/s).

Keywords: eVTOL; cross-flow fan; flow control; flow separation; lift coefficient

1. Introduction

With continuous advancements in electrical energy storage technologies and motor technologies, along with the widespread application of distributed electric drive systems, electric vertical takeoff and landing (eVTOL) aircrafts have attracted significant attention. They are a more environmentally friendly and safer mode of transportation [1]. The eVTOL aircraft offer numerous advantages, including low operating costs and flexible takeoff and landing capabilities, making them highly promising for urban air mobility (UAM) applications [2]. The current designs of eVTOL aircrafts predominantly include multi-rotor, fixed-wing hybrid multi-rotor, and tilt-rotor configurations [3,4]. However, these designs face challenges. Multi-rotor aircrafts exhibit good controllability, low cost, and high reliability, but they have limitations in payload capacity and flight speed. Tilt-rotor aircrafts offer high forward flight speeds and efficiency, but they encounter stability issues during tilting transitions, control challenges, and safety risks. Fixed-wing hybrid multi-rotor aircrafts combine the benefits of multi-rotor and tilt-rotor aircraft designs, offering good controllability and relatively higher flight efficiency [5]. Nonetheless, they suffer from additional dead weight, reducing payload capacity and requiring larger wing space [6].

Currently, there is an urgent need to explore quieter and more efficient eVTOL aircraft solutions tailored for UAM. Therefore, proposing a new eVTOL aircraft design aimed at enhancing safety, reducing noise levels, and improving propulsion efficiency holds great significance.

Currently, most eVTOL aircrafts utilize propellers as their primary lift and propulsion components. However, compared to wings, propellers suffer from a low weight–power ratio and high noise levels as lift components, and they lack the ability to achieve vertical takeoff and landing as propulsive components [7]. In recent years, researchers have explored integrating lift and thrust into a single system, with one prominent approach being the integration of propulsive systems into the wings or fuselage [8]. This approach allows for coupling wing aerodynamics with the propeller slipstream, reducing induced drag and reducing structural weight, further improving the aircraft's lift-to-drag ratio and flight performance. Furthermore, boundary layer suction has been shown to reduce power levels and jet noise by minimizing jet dissipation, thereby enhancing takeoff and landing performance [9]. This concept has been incorporated in conceptual design studies of various blended wing body configurations [10]. Moreover, the enhancement of Boundary Layer Ingestion (BLI) has been observed in several aircraft design studies, ranging from NASA's N3-X concepts to the MIT D-8 configuration [11].

The propulsive wing has attracted widespread attention as an important representative of integrated lift and propulsion design. The cross-flow fan (CFF) is a vital component for accelerating airflow within the propulsion wing system. Recently, there has been considerable interest in utilizing the CFF as a propeller or flow control device in aircraft applications. The CFF is suitable for integration along the span of an aircraft wing, due to its favorable two-dimensional flow characteristics, resulting in uniform inflow and outflow along the span [12]. Compared to helicopters, propulsive wing aircrafts demonstrate higher flight efficiency, with helicopters generating a power loading of 75 N/kw at cruising speed, while cross-flow fan aircrafts generate a power loading of approximately 250 N/kw during forward flight, because the rotor must also generate the required lift, whereas for the cross-flow fan aircraft, the wings generate the required lift, but the flight weight-to-power ratio of wings is greater than that of rotors. These characteristics make it an attractive candidate for distributed propulsion systems and flow control devices in eVTOL aircrafts [13]. An extensive analysis by Kummer [14] et al. and Ulvin et al. [15], validated through wind tunnel experiments and simulations, respectively, showcases the aerodynamic characteristics of propulsive wings. It is noteworthy that when the CFF's rotational speed reaches a certain value, the propulsive wing achieves a sufficient thrust-to-gravity ratio to enable hovering. Perry et al. [16] demonstrated an 11.8% reduction in fuel consumption through wind tunnel experiments and CFDs analysis, highlighting the feasibility of applying propulsive wings for eVTOL. However, two issues should be noted. Firstly, most studies on propulsive wings have relied on the CFDs method, and although they play a crucial role, further validation of their accuracy is required. Secondly, there are limited experimental studies investigating the relationship between propulsive wing aerodynamic performance and variables such as CFF rotational speed, angle of attack, and free-stream velocity, and they lack a deep understanding of its lift increase mechanism. In conclusion, to gain a better understanding of the flow field changes and lift increase mechanisms, it is essential to conduct wind tunnel experiments and CFDs simulations on key flight states of the novel eVTOL aircraft concept with propulsive wings. This will contribute to a more comprehensive understanding of the performance characteristics of propulsive wings and provide strong support for their optimization and improvement in practical applications.

Considering the relatively stable two-dimensional characteristics of the CFF, this article employs computational fluid dynamics (CFDs) simulations and wind tunnel experiments to investigate the aerodynamic characteristics of a two-dimensional propulsive wing. The primary objective is to analyze the aerodynamic forces and flow field characteristics on the propulsive wing, thereby revealing the lift enhancement mechanism and exploring the main parameters' relationship. This research lays the foundation for designing an eVTOL aircraft

with propulsive wings. The remaining sections of this paper are structured as follows: Section 2 introduces the conceptual design of an eVTOL aircraft with propulsive wings; Section 3 outlines the CFDs methods and experimental approaches; Section 4 analyzes the experimental and numerical simulation results; and finally, Section 5 presents the conclusions drawn from the research.

2. Conceptual Design and Research Object

Figure 1 depicts the eVTOL aircraft without crossflow wings. The integration of dual propeller systems on each axis ensures redundancy, enhances safety, and conserves space. However, shortcomings were noted in both its endurance and forward flight performance during test flights. However, efficiency is compromised by aerodynamic interference between the upper and lower propellers, while propeller lift counteracting gravity necessitates improvements to enhance the forward flight efficiency.

Figure 1. Image of eVTOL aircraft with a maximum takeoff weight of 350 kg. The maximum forward speed is 60 km/h and the endurance is 35 min. The payload is 80 kg and seats 1 person.

To enhance the forward flight speed and endurance performance of the aircraft, a conceptual design featuring the propulsive wings for the eVTOL aircraft was proposed. The schematic diagram is illustrated in Figure 2. The propulsive wing is positioned above the fuselage at a high angle of incidence (30°). Typically, conventional wings would stall during forward flight. However, due to the active control of separated flow on the wing's suction side by the rotating cross-flow fan, high angle of attack stalling is prevented, thereby enhancing the lift coefficient and increasing the propulsion force. Additionally, as the forward flight speed increases, the aircraft's pitch angle decreases, reducing the effective angle of attack of the propulsive wing and thus improving propulsion efficiency. During vertical flight, eight propellers provide lift for the eVTOL aircraft, with the aircraft's position and attitude controlled by varying propeller speeds. Upon reaching a safe altitude, the motor of the propulsive wing is activated during the forward flight, providing lift and propulsion. As the forward flight speed continues to increase, the lower propeller of the coaxial propeller device decelerates until the motor is deactivated. Subsequently, the upper propeller slows down to maintain the required lift and achieve a stable cruising speed at a fixed altitude. Throughout this process, the position and attitude of the eVTOL aircraft are controlled by the speed differential between the four sets of upper propellers [17].
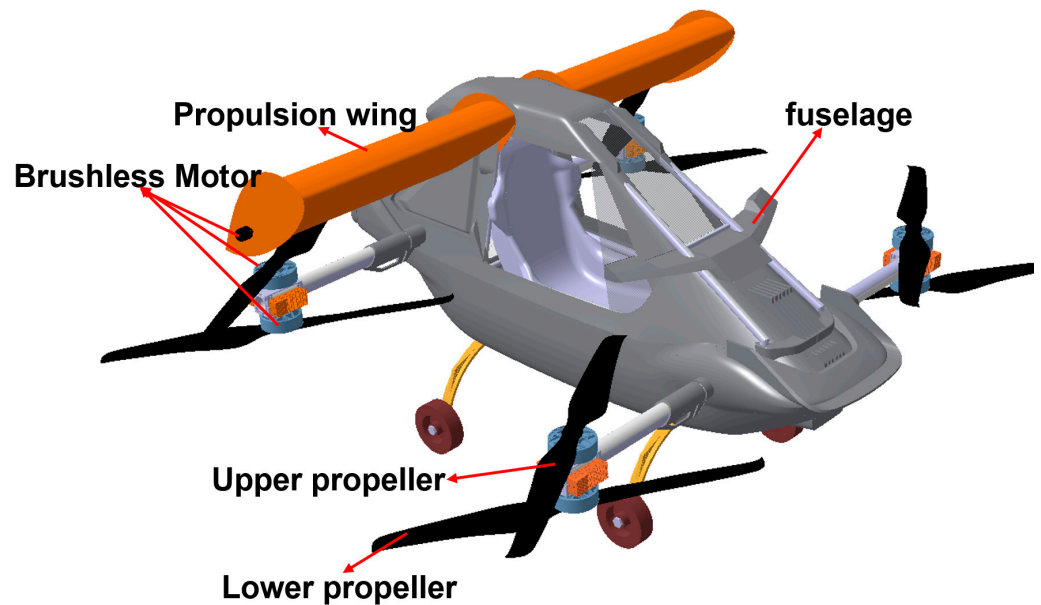
Figure 2. Design drawing of eVTOL aircraft with propulsive wing.

The eVTOL aircraft equipped with propulsive wings presents numerous advantages, including VTOL capability, high lift coefficients, improved flight efficiency, enhanced power performance, maneuverability, and reduced noise, and increased comfort for passengers. The details are as follows: (1) The propulsive wing features a substantial installation angle, resulting in a lift coefficient four to five times greater than that of a conventional wing at low airspeeds. With the same lift, the propulsive wing occupies less space, allowing for a more compact overall aircraft layout. (2) In forward flight, the propulsive wing predominantly generates lift, unloading eight propellers and feathering the lower propellers. This reduces aerodynamic interference between coaxial propellers and lowers propeller speed, thereby enhancing the flight efficiency [7]. (3) The propulsive wing contributes to the propulsion force, enhancing the cruising speed and acceleration of the eVTOL aircraft, significantly boosting the aircraft's power performance. (4) In forward flight, the attitude of the eVTOL aircraft is controlled by four upper propellers, which have high maneuverability and good stability, reducing the number of horizontal and vertical tails and optimizing the aerodynamic layout of the eVTOL aircraft. (5) Coaxial propellers generate noise from unsteady interferences between the upper and lower propellers and aerodynamic effects. In contrast, the blades of the propulsive wing are located inside the wing, resulting in significantly reduced aerodynamic noise compared to conventional propellers [18]. By unloading the propellers through the propulsive wing, the aircraft's noise is reduced, enhancing passenger comfort.

To verify the feasibility of the conceptual design for eVTOL aircrafts with propulsive wings and to analyze its working principle, CFDs calculations and wind tunnel experiments are conducted. The airfoil design is shown in Figure 3. It incorporates a truncated Gottingen 570 airfoil with a partially embedded CFF along the trailing edge. To control the flow direction, a deflector is positioned behind the CFF. The height of the CFF surpasses that of the suction surface of the airfoil to enhance the inspiratory capacity, thereby leading to improved performance. The housing comprises a primary vortex cavity, located counterclockwise of the outlet, and a secondary vortex cavity, located directly opposite to the primary one. The inclusion of these cavities can enhance fan performance by allowing the two eccentric vortices to occupy distinct cavities.
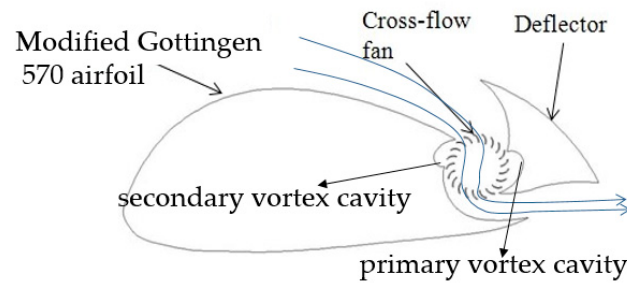
Figure 3. Airfoil of the propulsive wing.

The lift coefficient, drag coefficient, and torque coefficient of the propulsive wing are defined as

$$C_l = \frac{F_l}{1/2\rho U_\infty{}^2 Lc} \tag{1}$$

$$C_d = \frac{F_d}{1/2\rho U_\infty{}^2 Lc} \tag{2}$$

$$C_m = \frac{P/\omega}{1/2\rho U_\infty{}^2 rLc} \tag{3}$$

where F_l, F_d, P are the lift, drag and required power of the propulsive wing, respectively; ρ is the density and c is the chord length of the airfoil. When C_d is positive, the propulsive wing exhibits drag, whereas when C_d is negative, it manifests as propulsion force. L is the span length, and U_∞ is the free-stream velocity.

To describe the suction ability of the cross-flow fan, the definition of advance ratio (u) is introduced, i.e., the ratio of fan tip speed (U_f) to free-stream velocity (U_∞).

$$u = \frac{U_f}{U_\infty} = \frac{\omega r}{U_\infty} \tag{4}$$

3. Research Methods

3.1. CFDs Methods

3.1.1. Solution Method

The unsteady Reynolds-Averaged Navier–Stokes method (URANS) is employed in the CFDs model to simulate the incompressible flow field around the propulsive wing [19,20], employing identical conditions to those of the experimental setup. The governing equations are as follows:

$$\rho \frac{\partial(u_i)}{\partial x_i} = 0 \tag{5}$$

$$\rho \frac{\partial u_i}{\partial t} + \rho \frac{\partial(u_i u_j)}{\partial x_j} = -\frac{\partial p}{\partial x_i} + \frac{\partial}{\partial x_j}\left[\mu\left(\frac{\partial u_i}{\partial x_j} + \frac{\partial u_j}{\partial x_i}\right)\right] + F_i \tag{6}$$

where ρ is the density, $i = 1, 2$ represents coordinate axes, respectively, u is the velocity, p is the static pressure, and F_i is the volume force.

The flow inside the cross-flow fan can be characterized as two-dimensional viscous turbulent flow, where the rotation of the blades and the curvature of the surface contribute to the complexity of the flow within the fan. Additionally, factors such as the number of blades in the fan and the duct's flow diffusion can induce flow separation and secondary flow. The Realizable k-ε model is employed to capture the complex turbulence [21,22], with the transport equations for k and ε as follows:

$$\frac{\partial(\rho k)}{\partial t} + \frac{\partial(\rho k u_i)}{\partial x_i} = \frac{\partial}{\partial x_j}\left[\left(\mu + \frac{\mu_t}{\sigma_k}\right)\frac{\partial k}{\partial x_j}\right] + G_k - \rho\varepsilon \tag{7}$$

$$\frac{\partial(\rho\varepsilon)}{\partial t} + \frac{\partial(\rho\varepsilon u_i)}{\partial x_i} = \frac{\partial}{\partial x_j}\left[\left(\mu + \frac{\mu_t}{\sigma_k}\right)\frac{\partial\varepsilon}{\partial x_j}\right] + \rho C_1 E\varepsilon - \rho C_2 \frac{\varepsilon^2}{k + \sqrt{\nu\varepsilon}} \tag{8}$$

The finite volume method with second-order accuracy was used for the spatial discretization. The Semi-Implicit Method for Pressure Linked Equation (SIMPLE) algorithm [23] based on pressure correction was used to solve the governing equation. Considering the accuracy and economy of the calculation, the rotation angle of each time step is set to $1°$.

3.1.2. Mesh Refinement

Figure 4 illustrates the computational domain, boundary conditions, and other settings for the simulations. In the forward flight (Figure 4a), the left side represents a uniform velocity inlet, the right side is a pressure outlet, and the top and bottom are symmetric boundaries. Since the analysis involves the rotation of the fan, sliding mesh technology is established for computation. The main airfoil and deflector adopt no-slip boundary conditions, the circular region inside the fan and the external flow fields are static zones, and the region around the blades is a rotating zone (Figure 4b), partitioned using unstructured meshes. The mesh at the propulsive wing is shown in Figure 4d. To accurately capture the details of the wing's wake and enhance computational accuracy, the mesh near the airfoil is refined.
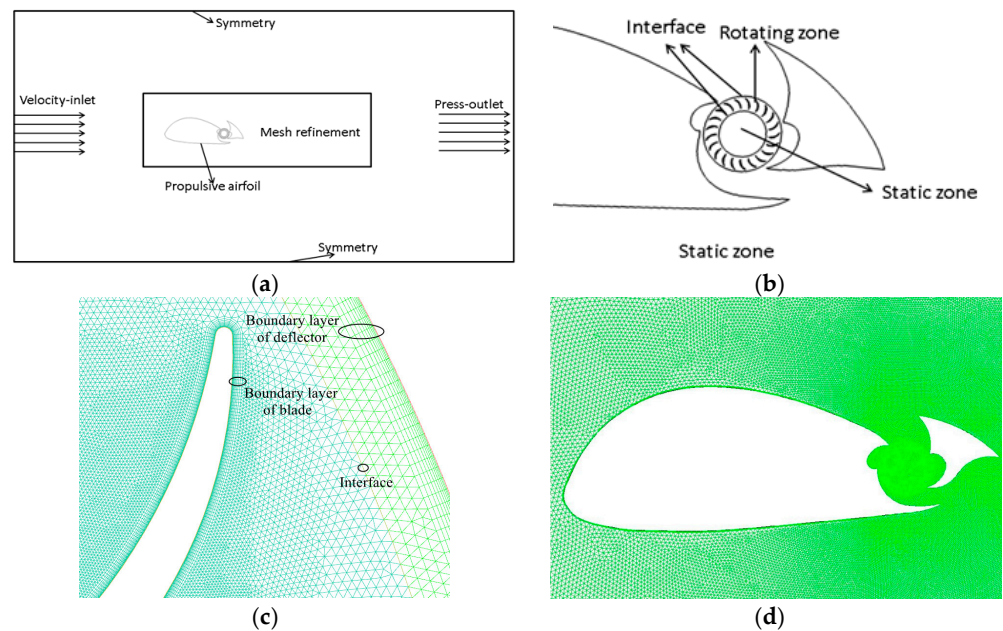

Figure 4. Computational domain and sliding mesh. (**a**) Computational domain partitioning. (**b**) Rotation zone and static zone. (**c**) Boundary layer grid. (**d**) Overall unstructured mesh.

### 3.2. Experimental Methods
3.2.1. Experimental Subject

The experimental model of the propulsive wing is illustrated in Figure 5, processed using acrylic material. It comprises a main wing, a deflector, a CFF, and two plates. The original Gottingen 570 airfoil has a chord length of 600 mm, and the CFF is positioned at 80% of the airfoil's chord. The fan has a diameter of 80 mm, 21 blades, and the outlet height measures 35 mm. The aspect ratio of the propulsive wing is small, and the three-dimensional effect is significant, so two end-plates are installed at the wing ends to make a 2D flow over the airfoil. The motor driving the CFF is securely mounted on one of the plates. Additionally, adjusting holes are provided on the plate at $10°$ intervals to facilitate effective angle of attack adjustments during experiments.
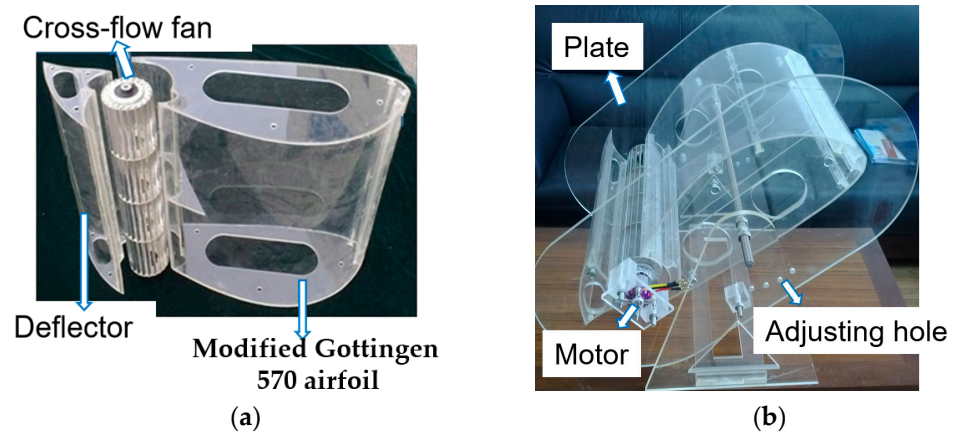
Figure 5. Experimental model of the propulsive wing. (**a**) breakdown diagram. (**b**) Overall diagram.

3.2.2. Experimental Setup

An experimental setup for aerodynamic measurements of the propulsive wing was devised, as depicted in Figure 6. It consists of five main components: the propulsive wing system, measurement system, power system, rotational speed control system, and low-speed return flow wind tunnel. The propulsive wing is mounted on a six-component balance for measuring aerodynamic forces and moments. The CFF is driven by a 1.3 kW DC motor, and its rotational speed is controlled by an electronic speed controller. The motor is connected directly to the fan without a gearing system. For enhanced experimental safety, the maximum speed of the CFF is limited to 3000 r/min. The test section of the wind tunnel measures 3.2 m × 2.4 m, with a maximum wind speed of 50 m/s. The basic specifications of the DC stabilized power supply include an input AC voltage of AC220V ± 10%, frequency of 50 Hz, safe operating voltage range of 0–60 V, and safe operating current range of 0–100 A. The frontal area of the experimental platform is relatively small, which reduces aerodynamic interference with the test model. Additionally, adjustments to the position of the installation holes can be made quickly to adjust the incoming flow angles of attack, meeting the varied requirements of the experiment.
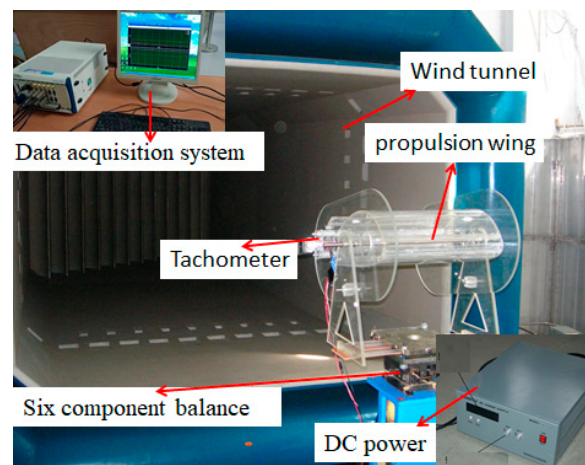
Figure 6. Aerodynamic force measurement test bench.

3.2.3. Experimental Principle and Scheme

The basic principle of the experiment is to use wind tunnel experiments to simulate the flow field of the propulsive wing under different operating conditions. A six-component balance is used to measure the aerodynamic data such as lift, drag, and pitching moment, and these dynamic data are recorded through a data acquisition system. The experimental challenge lies in accurately obtaining the torque data required by the propulsive wing.

Considering that mechanical losses of the motor can affect the measurement of the power required by the propulsive wing, baseline data are initially collected by measuring the voltage U_e and current I_e of the power supply cabinet at different speeds without installing the cross-flow fan. Subsequently, the cross-flow fan is installed for measurement, and the voltage U and current I of the power supply cabinet are recorded to calculate the actual power consumption. The difference between the two sets of values yields the final power experimental data, while the required torque can be determined through the corresponding formula.

$$P_{text} = IU - I_eU_e \tag{9}$$

$$Q_{text} = P_{text}/\Omega \tag{10}$$

Numerous factors affect the aerodynamic performance of the propulsive wing, primarily including forward flight speed, rotational speed, and angle of attack, with these three factors exhibiting coupling effects during flight. To analyze the impact of individual factors on aerodynamic characteristics, this experiment employed a single-variable control method, systematically investigating the effects of these parameters on the aerodynamic performance of the propulsive wing. Thus, experiments were conducted under different rotational speeds (0 rpm, 1000 rpm, 2000 rpm, 3000 rpm), free-stream velocities (3 m/s, 5 m/s, 7 m/s, 9 m/s, 11 m/s), and angles of attack (0°, 10°, 20°, 30°, 40°).

3.2.4. Analysis of Experimental Setup Interference

(1) Analysis of experimental stand interference

During wind tunnel testing, the use of an experimental stand is inevitable. However, the stand itself generates additional aerodynamic forces and alters the aerodynamic forces acting on the experimental subjects. This leads to deviations in the measured values, causing them to deviate from the true values and resulting in a system error. To address this issue, a separate experiment was conducted without the cross-flow fan to quantify the interference caused by the experimental stand, as depicted in Figure 7. The obtained interference values are subtracted from the subsequent experiments. This correction minimizes the influence of the experimental stand on the measurements, ensuring greater accuracy of the results.

(**a**)   (**b**)
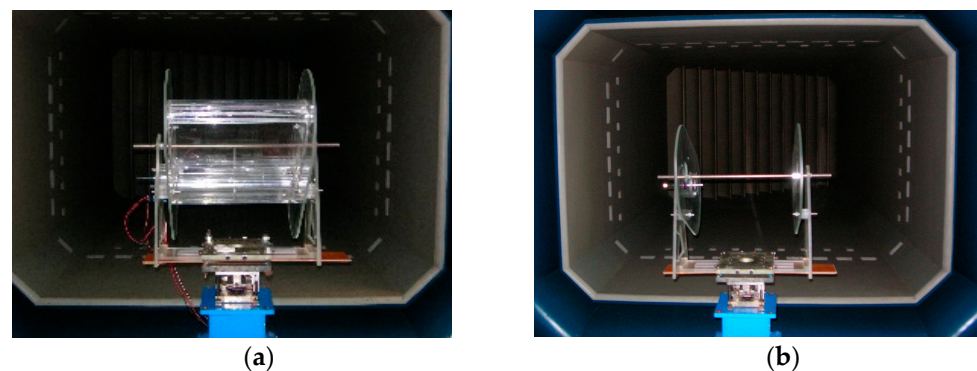
Figure 7. Experimental stand interference: (**a**) with airfoil, (**b**) without airfoil.

(2) An uncertainty analysis.

Measurement errors mainly stem from the measurement of rotational speed and aerodynamic force, falling under the category of random error. The magnitude and sign of the error fluctuate irregularly. Due to the unsteady flow field around the propulsive wing, it is difficult to adjust the experimental rotational speed to a fixed value. The fluctuation range of the rotational speed is within 1%, resulting in fluctuations in the experimental results. After stabilizing the rotational speed, data are collected over a 15 s period. The first and last half cycles are periodically removed, and the remaining data are averaged. Within the collected data, the standard deviation of the average value for each period is 4.8%. To minimize random errors, a method of dividing the time period and conducting three

separate experiments was adopted. The average value of these experiments is taken as the final measurement value. The standard deviation of the average value across the three experiments was 12%. This method reduces the impact of random errors and improves the reliability of the measurement results. It should be noted that the number of experiments needs to be increased to improve their repeatability.

3.3. Verification of CFDs Methods

3.3.1. Grid Independence Verification

Before conducting CFDs calculations, it is necessary to validate grid independence. The main feature of the propulsive wing is the rotation of the cross-flow fan, which results in a relatively higher velocity compared to the main wing profile and its smaller size. Therefore, the primary component affecting the computational results is the cross-flow fan. Significant mesh factors affecting the computational results include the quality of the boundary layer mesh and mesh density.

There is complex turbulence around the blades of the cross-flow fan, and the quality of the boundary layer mesh significantly impacts the computational results. According to the computational experience in the literature [24], the height (d1) of the first boundary layer mesh is set to 0.00001 m, 0.00002 m, 0.00003 m, and 0.00006 m, respectively. The growth rate of the grid size is 1.1, and the total number of boundary layers is 5. The lift growth rate ($Lift\_rate$) of the calculation is shown in Equation (11), where $L_{Newmesh}$ is the lift of the new grid and $L_{Oldmesh}$ is the lift of the last grid. Figure 8 illustrates the impact of different first-layer mesh heights on the calculation results, with the cross-flow fan rotating at 3000 r/min and a forward velocity of 10 m/s. It can be seen that as the height of the first-layer grid increases, the impact on computational accuracy increases, but from 0.00002 m to 0.00001 m, the computational accuracy remains basically unchanged. Therefore, it is considered that when the grid height reaches d_1 = 0.00002 m, the calculation results are considered converged.

$$Lift\_rate = \frac{L_{Newmesh} - L_{Oldmesh}}{L_{Newmesh}} \times 100\% \tag{11}$$
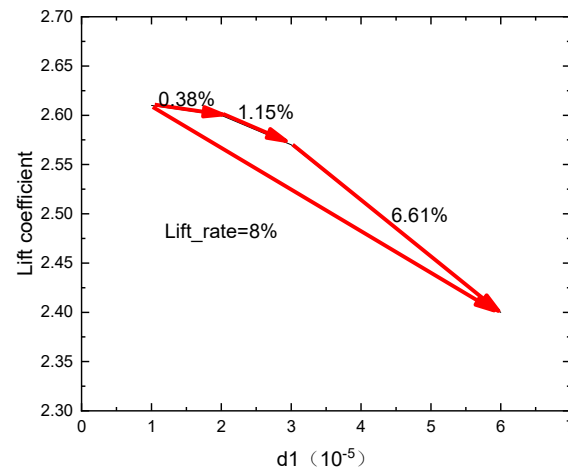
Figure 8. Relationship between lift coefficient of the propulsive wing and the height of the first grid layer, with the cross-flow fan rotating speed of 3000 r/min, an angle of attack of 40°, and a free-stream velocity of 10 m/s.

Insufficient mesh quantity affects computational accuracy, while excessive mesh quantity impairs computational efficiency. Therefore, it is necessary to select an appropriate mesh density [25]. When investigating the influence of mesh density on computational results, five distinct mesh densities were utilized, specifically 0.5 million (overall sparse), 1 million (baseline), 1.5 million (rotation zone refinement), 2 million (encryption zone refinement), and 2.5 million (overall refinement). Figure 9 illustrates the computational

results and iteration errors of the propulsive wing under different mesh densities, with a cross-flow fan rotating speed of 3000 r/min, an angle of attack of 40°, and a free-stream velocity of 10 m/s. It can be observed that the mesh density around the cross-flow fan significantly affects the computational results, followed by the encryption area. Considering both computational accuracy and efficiency, 1.5 million meshes were selected for calculating the aerodynamic performance of the propulsive wing.
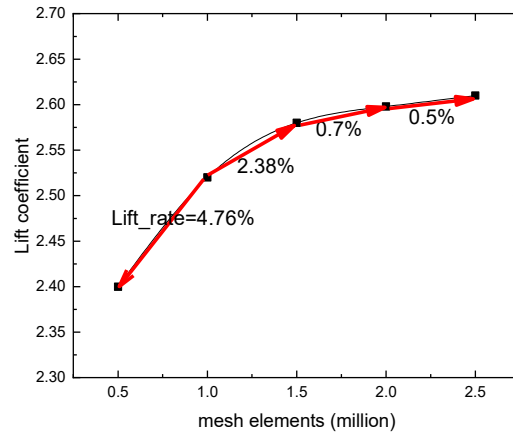
Figure 9. Relationship between lift coefficient of propulsive wing and the mesh density, with a cross-flow fan rotating speed of 3000 r/min, an angle of attack of 40°, and a free-stream velocity of 10 m/s.

3.3.2. Result Comparison Verification

Figure 10 presents a comparison between the calculated and experimental CFDs values of aerodynamic forces for the propulsive wing at a 10° angle of attack. The trends and results show a basic agreement with the experimental data, with a maximum error of no more than 15%. These discrepancies arise partly from the influence of the remaining three-dimensional effects on the aerodynamic performance of the propulsive wing and partly from errors between the experimental model and the CFDs computational model. Based on the error results, we believe that the 2D CFDs result and wind tunnel result are reliable. Overall, the experimental results validate the reliability of the CFDs calculation method developed in this study for the propulsive wing.
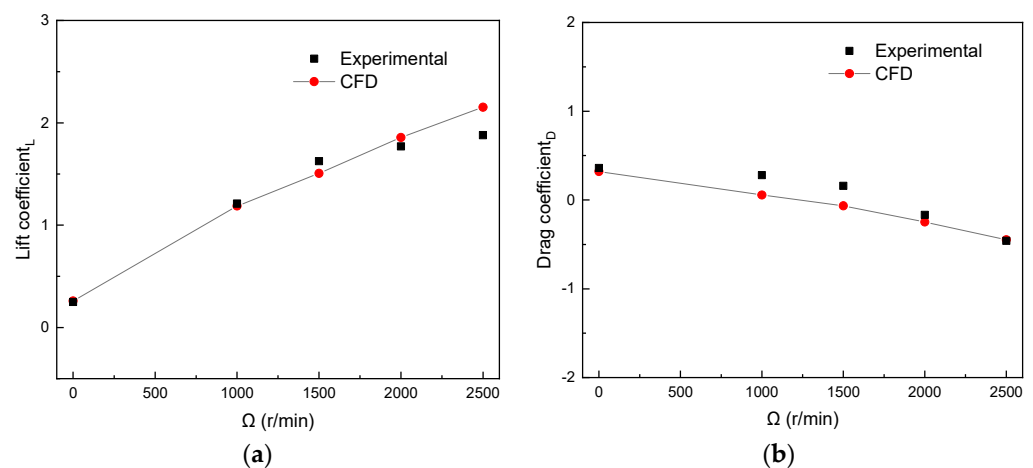

Figure 10. Comparison of CFDs calculation and experimental results at an angle of attack of 10° and a free-stream velocity of 10 m/s. (**a**) Lift coefficient. (**b**) Drag coefficient.

4. Results Analyze

4.1. Mechanism of Propulsive Wing

4.1.1. Aerodynamic Analysis

Figure 11 compares the aerodynamic coefficients of the propulsive wing at different angles of attack when the free-stream velocity is 3 m/s and 11 m/s. It can be seen that the aerodynamic coefficients of the propulsive wing with the fan turned off are similar to those of the original Gottingen 570 airfoil, where the error less than 15% and both are below 1.5. However, the aerodynamic coefficients of the propulsive wing are slightly lower than those of the original airfoil, mainly due to the influence of three-dimensional effects, with spanwise flow affecting the lift coefficient. When the cross-flow fan rotates at 3000 r/min, the lift coefficient increases rapidly with increasing angle of attack. At an angle of attack of 40°, the lift coefficient reaches 7.6, with a propulsion force coefficient of 7.1. When the free-stream velocity is 11 m/s, the rotation speed is 0 r/min, and the angle of attack is 30°, stalling of the propulsive wing occurs. However, when the speed is 3000 r/min, the lift and drag curve continues to increase. This indicates that the cross-flow fan can actively control the airflow around the propulsive wing, causing the airflow on the wing surface to reattach and thereby improving the lift performance of the propulsive wing. It is worth noting that the aerodynamic performance of the propulsive wing at different angles of attack is significantly affected by the rotational speed of the cross-flow fan. This reflects the differences in aerodynamic performance between the propulsive wing and conventional airfoils, as well as the important role of the cross-flow fan in its aerodynamic characteristics [26].
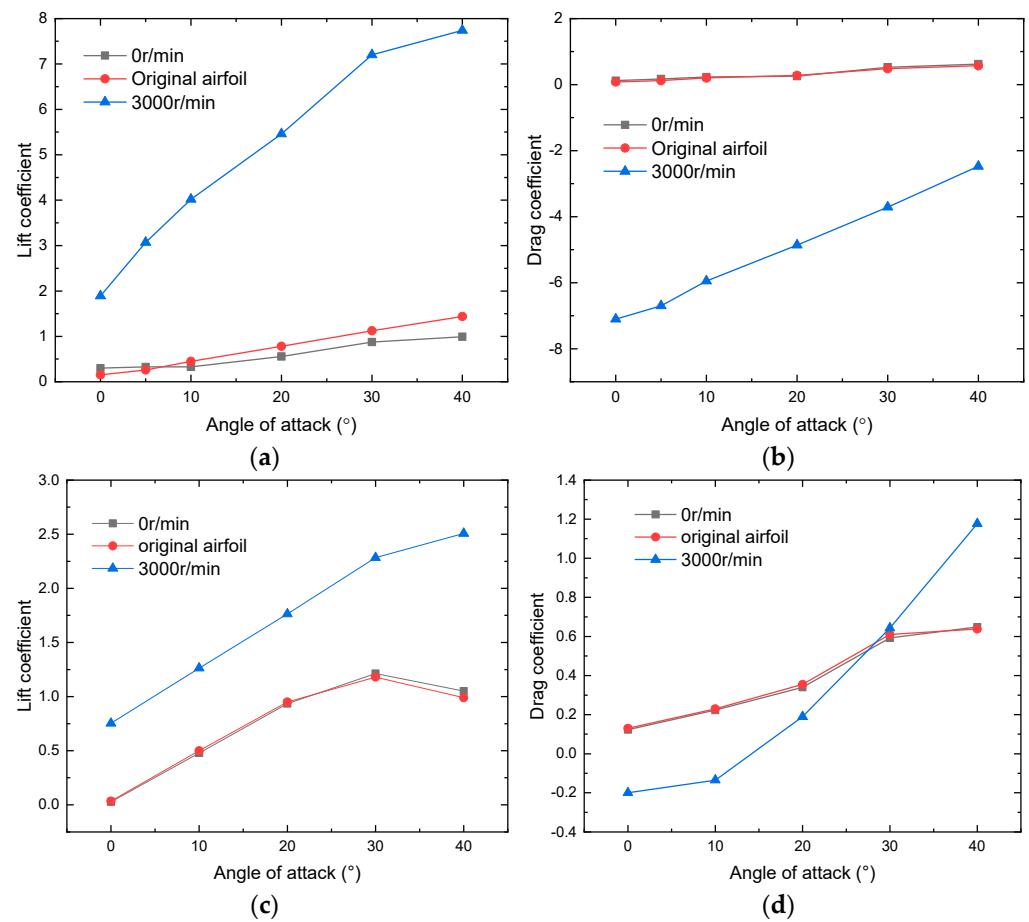

Figure 11. Aerodynamic coefficient by wind tunnel. (**a**) Lift coefficient at 3 m/s. (**b**) Drag coefficient at 3 m/s. (**c**) Lift coefficient at 11 m/s. (**d**) Drag coefficient at 11 m/s.

4.1.2. Analysis of High Angle of Attack Stall Mechanism

To gain further insight into the mechanism behind the high lift performance of the propulsive wing at high angles of attack, the time-averaged streamlines were further analyzed when the cross-flow fan rotates at 3000 r/min and when it remains stationary, as shown in Figure 12. Evidently, when the fan is stationary, severe airflow separation occurs on the suction surface of the airfoil, leading to complete stall of the wing. Large vortex regions can be observed, and the wake of the airfoil is significantly disturbed, which severely affects the aerodynamic characteristics of the wing. In contrast, when the fan rotates, a strong suction effect is generated, introducing a large amount of turbulence into the cross-flow fan and promoting stable airflow attachment on the airfoil surface. This effectively eliminates the phenomenon of airflow separation on the suction surface. Comparing the two cases, when the fan is not rotating, the suction surface of the airfoil experiences large areas of high pressure due to severe airflow separation, as shown in Figure 13a. Conversely, when the fan rotates, the airflow velocity on the upper surface of the airfoil increases, resulting in reduced pressure, as depicted in Figure 13b. Consequently, the pressure difference between the upper and lower surfaces becomes more significant, thereby improving the lift performance of the propulsive wing. By attracting air onto the suction surface, energizing it, and expelling it from the trailing edge of the airfoil, the CFF effectively prevents flow separation at high angles of attack and achieves a relatively high lift coefficient.


(**a**)	(**b**)
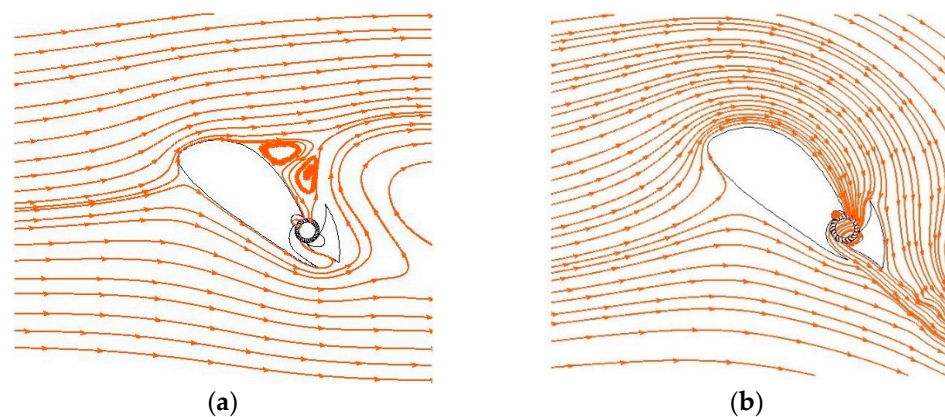
Figure 12. Time-averaged streamlines at 40° angle of attack and a free-stream velocity of 10 m/s by CFDs method. (**a**) The stationary CFF. (**b**) The 3000 r/min CFF.

(**a**)	(**b**)
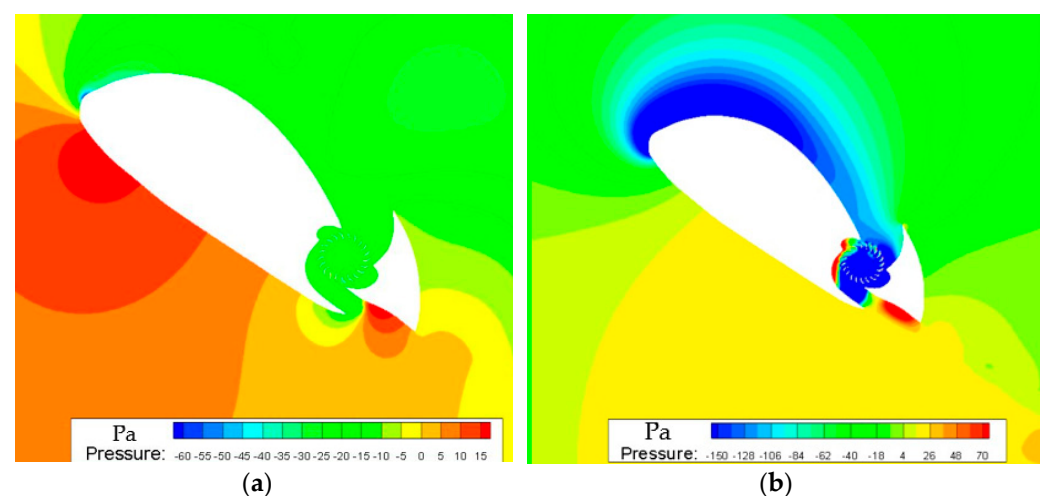
Figure 13. Contour pressure at 40° angle of attack and a free-stream velocity of 10 m/s by CFDs method. (**a**) The stationary CFF. (**b**) The 3000 r/min CFF.
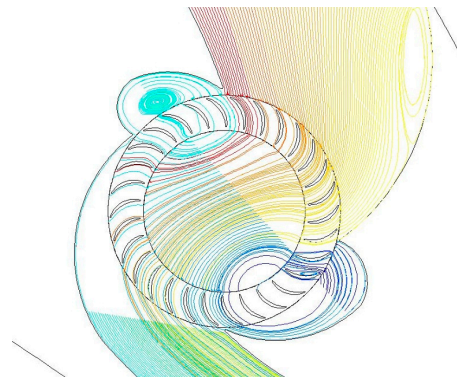
4.1.3. Eccentric Vortex Analysis

After in-depth research, it was found that the fan of the propulsive wing not only implements boundary layer control technology by ingesting the airflow above the wing, causing the airflow to reattach to the suction surface and reducing airflow separation, but also generates an eccentric vortex due to the rotation of the fan, thereby producing vortex-induced lift and thrust. When the fan starts to rotate from rest, the fluid near the blades begins to undergo unsteady motion, resulting in a change in total pressure around the circumference of the impeller [27]. Simultaneously, the circulation of the airflow in contact with the fan blade boundary increases, resulting in the generation of vortices at the wingtip of the blade. As shown in Figure 14, due to the viscosity of the airflow and its high-speed flow, some vortices will move and dissipate downstream of the propulsive wing with the airflow, while another portion of the vortices will move inward and dissipate inside the fan. The high-speed rotation of the fan blades confines the vortices inside, forming two elliptical vortex clusters. Consequently, the vortices continuously generated by the fan blades move inward, and during this process, the vortices continuously dissipate until reaching a dynamic equilibrium, forming two stable vortex clusters. Once the flow field reaches a stable state, these elliptical vortices' aggregation areas also become stable, with the vortices' magnitude in their core regions approaching twice the rotational speed of the fan.
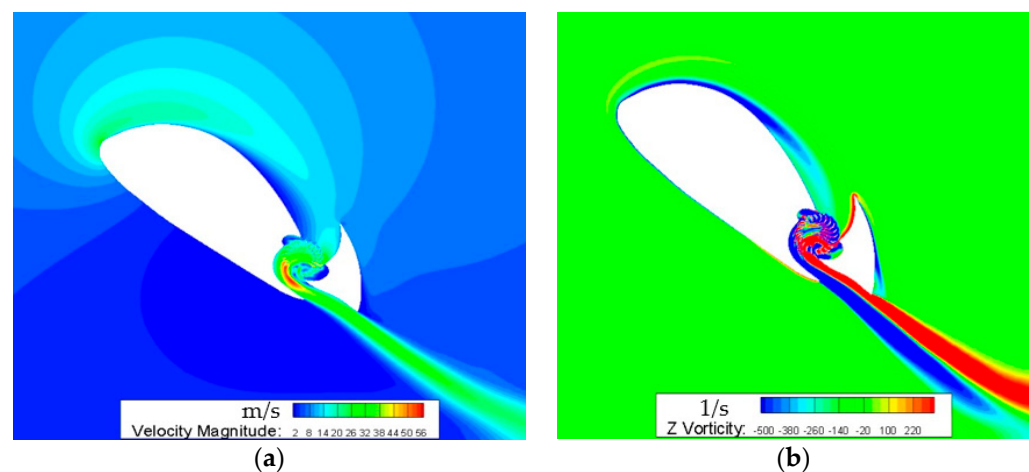
Figure 14. Contour velocity and contour vorticity, with a cross-flow fan rotating speed of 3000 r/min, an angle of attack of $40°$, and a free-stream velocity of 10 m/s. (**a**) Contour velocity. (**b**) Contour vorticity.

Through the calculation analysis in Appendix A, it is evident that throughout the flow process from the inlet to the outlet of the propulsive wing, the total pressure along the circumference of the fan varies, and the airflow exhibits vortices. Vortices are formed inside the fan, and there are two vortices due to the presence of both the inlet and outlet openings, which can be seen in Figure 15.

Through the calculation analysis in Appendix A, for any closed object in a flow field, the lift is determined by the density of the flow field, the incoming flow velocity, and the circulation around the object. Since the flow field at the propulsive wing fan is incompressible, with density being constant, the main factors influencing the lift of the propulsive wing are the incoming flow velocity and the circulation around the propulsive wing.

Figure 15. Detailed image of the eccentric vortex of the propulsive wing by CFDs method with a cross-flow fan rotating speed of 3000 r/min, an angle of attack of 40°, and a free-stream velocity of 10 m/s.

4.1.4. Performance Impact Analysis

The preceding analysis indicates that the aerodynamics of the propulsive wing are influenced by the airflow pattern around the wing and the intensity of the eccentric vortex. The airflow pattern around the wing is contingent upon the incoming velocity and the suction capability of the fan, while the intensity of the eccentric vortex is closely related to the circulation. Figure 16 illustrates the streamlined distribution under different advance ratios. With an increase in the advance ratio, the vortices on the upper surface of the wing diminish, and the airflow on the upper surface of the wing is notably drawn downward and reattaches to the surface. As the advance ratio further increases, the intensity of the eccentric vortex generated by the fan rises, further enhancing the lift. Simultaneously, the eccentric vortex inside the fan moves upward and to the right and diminishes in size, leading to an enlargement of the flow channel area and thereby augmenting the suction capability of the fan [14]. The lift coefficient of the propulsive wing is directly correlated with the advance ratio, which reflects the suction capability of the cross-flow fan. If the advance ratio is sufficiently large, the cross-flow fan can draw the separated airflow down, implying that even at significantly high angles of attack (up to 40°), the wing will not stall, and a substantial lift coefficient can be achieved.

u = 1.01

u = 1.68

u = 3.37

u = 6.57
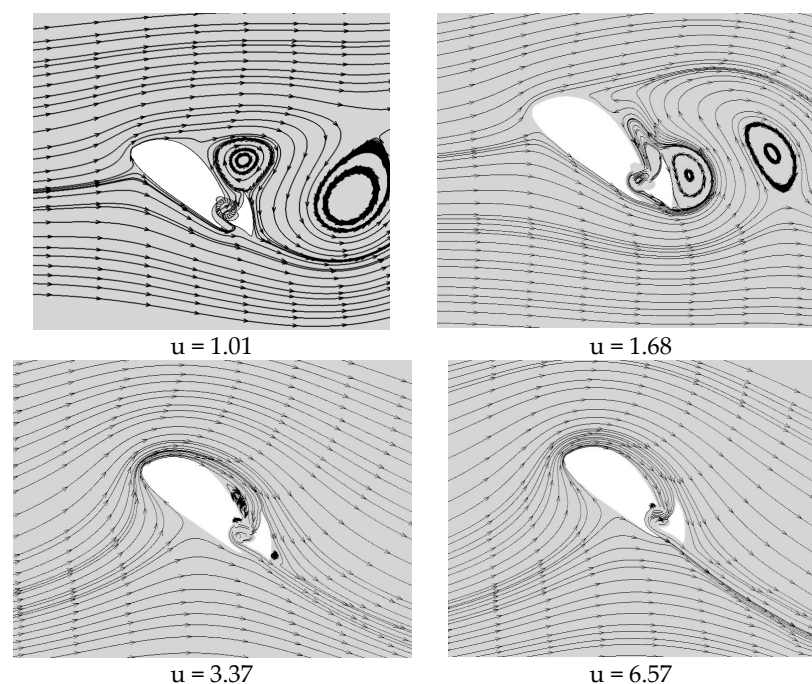
Figure 16. Streamlines at different advance ratio by CFDs method at 40° angle of attack and a free-stream velocity of 10 m/s.

4.2. Relation between Aerodynamic Performance and Angle of Attack

The main characteristic of the propulsive wing is its capability to maintain non-stalling behavior at high angles of attack, accompanied by a significantly large maximum lift coefficient (CLmax). Therefore, it is necessary to investigate the aerodynamic performance of the propulsive wing concerning the angle of attack. Figure 17a illustrates the relationship between the lift coefficient and the angle of attack. When the free-stream velocity and fan rotation speed remain constant, the lift coefficient generally increases linearly with the angle of attack, akin to the trend observed in conventional wing profiles. This suggests that the suction surface of the propulsive wing undergoes minimal flow separation even at high angles of attack under the influence of the fan. In contrast, conventional wing profiles experience stall when the angle of attack exceeds 15°. The acceleration effect of the CFF delays the separation of airflow over the suction surface, leading to an increase in the maximum lift coefficient (CLmax). However, when the angle of attack reaches a critical threshold, the lift ceases to increase, indicating that the acceleration effect of the CFF is insufficient to reattach the separated airflow to the suction surface. Consequently, flow separation occurs on the upper surface, leading to a notable surge in drag. The slope of the lift coefficient curve varies at different fan rotation speeds, with higher speeds yielding a greater slope. This phenomenon primarily stems from the heightened fan rotation speed, which not only delays airflow separation but also enhances the strength of the eccentric vortices inside the fan. Moreover, the addition of an angle-adjustable deflector at the outlet would offer vectored propulsive force.
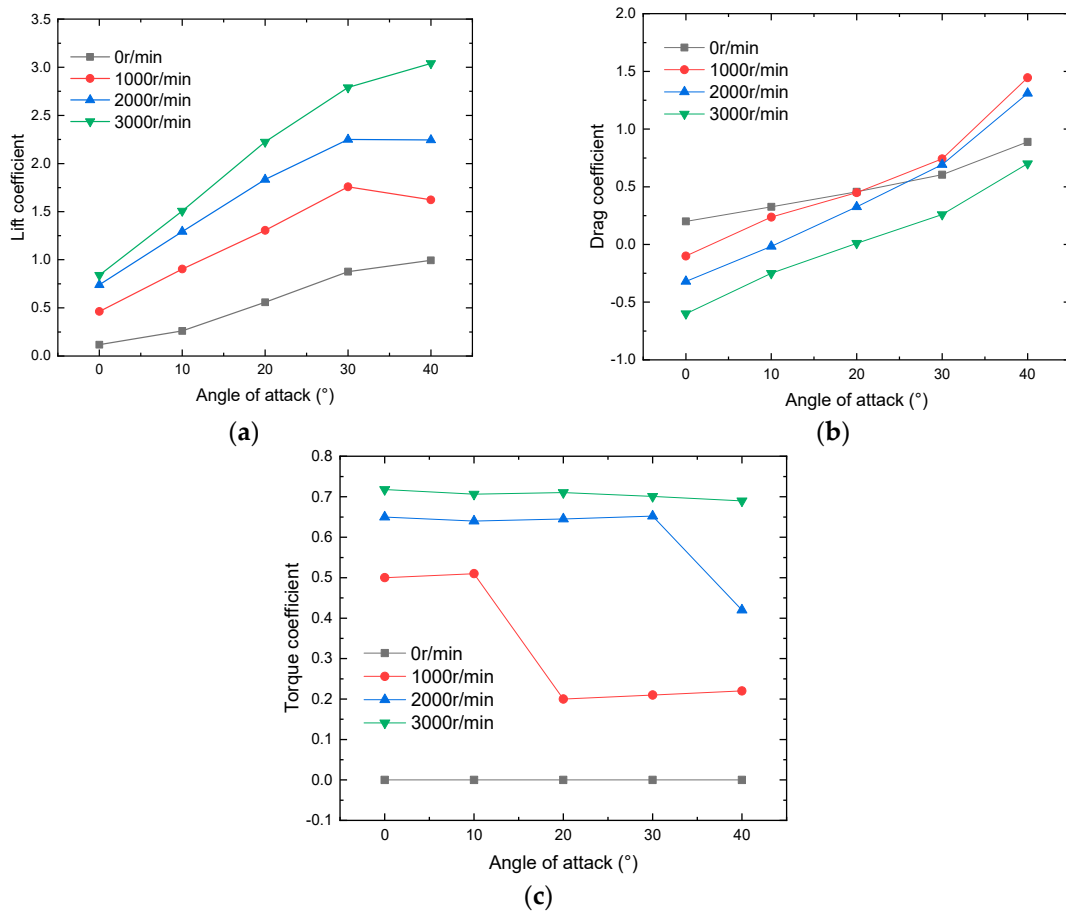
Figure 17. Aerodynamic coefficient of propulsive wing with different angles of attack ($V = 7$ m/s). (**a**) Lift coefficient by wind tunnel. (**b**) Drag coefficient by wind tunnel. (**c**) Torque coefficient by wind tunnel.

The drag composition of the propulsive wing differs significantly from that of conventional airfoils, as it introduces additional drag from the deflector and the cross-flow fan blade. However, measuring the drag on the fan blades presents challenges due to limited experimental conditions. The focus of this study is on analyzing the total drag of the propulsive wing. Figure 17b illustrates the relationship between the drag coefficient and the angle of attack. It is observed that with constant free-stream velocity and rotational speed, the drag coefficient (which represents the thrust coefficient when its negative value is considered) generally increases linearly with the angle of attack [28]. On the one hand, as the angle of attack rises, the windward side of the propulsive wing expands, resulting in increased drag. On the other hand, the direction of the high-speed jet shifts with changes in the angle of attack, leading to corresponding variations in the horizontal component, thereby increasing resistance and decreasing thrust. Moreover, higher rotational speeds correspond to smaller drag coefficients and steeper slopes of the drag coefficient. Traditional flow control techniques focus on reducing aerodynamic drag by minimizing wake area and disturbance. In contrast, the CFF demonstrates a more pronounced ability to mitigate wake disturbances. Furthermore, by altering the pressure distribution on the inner cavity surface, CFFs can significantly diminish the drag coefficient and even generate propulsive force.

The torque coefficient characterizes the power of the propulsive wing. The relationship between the torque coefficient and angle of attack is depicted in Figure 17c. When the free-stream speed and rotational speed are constant, the torque coefficient remains unchanged as the angle of attack increases. However, the lift coefficient gradually rises, leading to a significant increase in lift per unit power. This phenomenon primarily occurs because the mass flow rate entering the inlet remains relatively constant during the augmentation of the angle of attack, thereby maintaining the advance ratio. Consequently, the torque demand for the propulsive wing remains stable. At an angle of attack of 30° and a rotational speed below 2000 r/min, airflow separation may occur on the upper surface of the propulsive wing, resulting in a reduced torque coefficient. The lift coefficient loss of thick airfoils is not very sensitive to airflow separation at low forward speeds.

4.3. Relationship between Aerodynamic Performance and Rotational Speed

The control of fan rotation speed is the most direct and effective means of altering the aerodynamic characteristics of the propulsive wing. By adjusting the rotation speed of the CFF, the mass flow through the fan and the momentum of the jet can be modified, facilitating the circulation control of the propulsive wing. When the free-stream velocity and angle of attack are held constant, an increase in fan rotation speed leads to a higher advance ratio for the propulsive wing, consequently resulting in an increase in the lift coefficient, as depicted in Figure 18a. This phenomenon primarily arises from the augmentation of the cross-flow fan's suction capacity with the advance ratio, resulting in a more pronounced suction effect on the boundary layer. Additionally, similar to a rotor, as the rotational speed increases, the induced velocity also rises, amplifying the aerodynamic force generated by the cross-flow fan. As the advance ratio advances, the eccentric vortex inside the fan shifts towards the upper right corner, reducing the vortex core while expanding the flow channel area, further enhancing the cross-flow fan's suction capacity. Under conditions of high angle of attack, when the advance ratio falls below a certain critical value (wherein the free-stream velocity exceeds a specific threshold or the rotational speed is below a designated threshold), a severe air separation phenomenon occurs at the propulsive wing's leading edge, resulting in airfoil stall and thereby impacting the propulsive wing's aerodynamic characteristics. As the advance ratio gradually increases, the robust suction effect generated by the fan draws a substantial amount of turbulence onto the propulsive wing's suction surface, forming a stable laminar flow on the airfoil surface. This effectively prevents airflow separation at high angles of attack and concurrently enhances airflow velocity on the upper surface of the propulsive wing, thereby achieving a relatively high lift coefficient. When the rotational speed is fixed, a decrease in free-stream velocity corresponds to an increase in the lift coefficient. This is primarily attributed to the predominance of the aerodynamic force

generated by the propulsion blade at this juncture. As the free-stream velocity increases, the lift generated by the airfoil progressively becomes dominant. Consequently, the lift coefficient of the propulsive wing is higher at lower speeds.
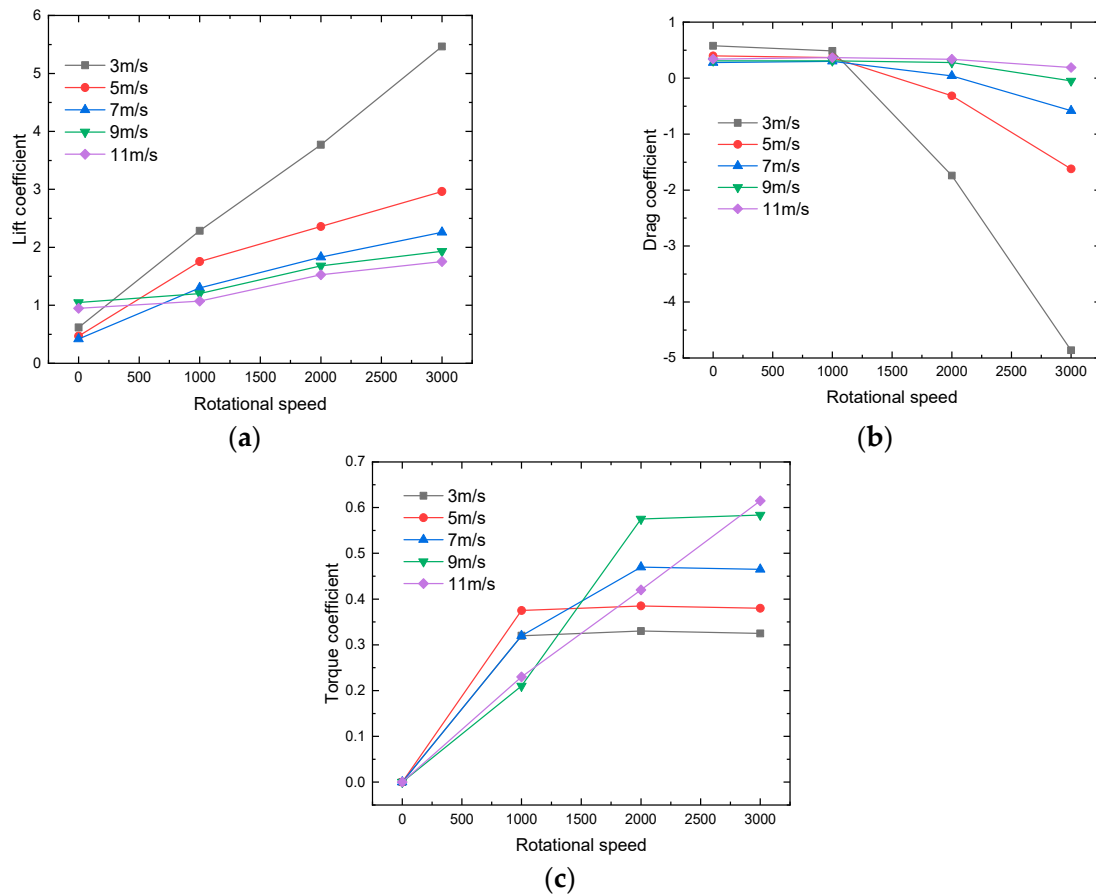
Figure 18. Aerodynamic coefficient of propulsive wing with different rotational speed ($\alpha = 20°$). (**a**) Lift coefficient by wind tunnel. (**b**) Drag coefficient by wind tunnel. (**c**) Torque coefficient by wind tunnel.

As illustrated in Figure 18b, at a constant inflow speed and angle of attack, the drag coefficient of the propulsive wing (the inverse being the thrust coefficient) tends to decrease (increase) as the fan's rotational speed rises. When the fan's rotational speed surpasses a certain critical value, the drag coefficient becomes negative, indicating the propulsion coefficient. For instance, when the free-stream velocity is 3 m/s and the fan's rotational speed is 3000 r/min, the drag coefficient reaches -6.3 at a $10°$ angle of attack, where the negative drag represents propulsion. The rationale behind this phenomenon lies in two key factors. Firstly, the mass flow through the CFF augments with the increase in the CFF's speed, resulting in high-speed airflow being expelled along the rear edge of the wing, consequently boosting propulsive force. Secondly, as the rotational speed increases, the blade rotation alters the pressure distribution on the wall of the arc groove of the propulsive wing, thereby reducing the pressure differential drag of the propulsive wing. When the free-stream velocity is less than 10 m/s, the drag coefficient decreases with the rotational speed, primarily due to the predominant aerodynamic force generated by the propulsion blade. The lower the free-stream velocity, the more pronounced the change in the drag coefficient. When the free-stream speed reaches 20 m/s and the wing angle of attack exceeds $30°$, the drag of the propulsive wings no longer varies with the increase in CFF rotational speed. At this juncture, the advance speed is relatively low, and the suction force of the CFF is insufficient to draw in separated airflow at high angles of attack.

The variation in the torque coefficient with rotational speed is depicted in Figure 18c. When the angle of attack remains constant, the torque coefficient of the propulsive wing gradually increases with increasing rotational speed, initially rising slowly, then sharply, and eventually stabilizing. Overall, the power required by the propulsive wing increases with the increase in CFF rotational speed. It is noteworthy that there exists a certain turning point in the torque coefficient in the process of change. This is primarily because when the advance ratio is relatively low, an airflow stall phenomenon occurs. With the enhancement in suction capacity, the airflow gradually stabilizes, and consequently, the torque coefficient tends to stabilize accordingly. Power is primarily utilized to accelerate the airflow through the flow channel, mitigate friction loss of the boundary layer, and maintain the strength of the internal eccentric vortex. The higher the rotational speed, the more significant the acceleration effect on the airflow in the flow channel and the greater the intensity of the eccentric vortex, resulting in an increase in the power.

*4.4. Relationship between Aerodynamic Performance and Free Stream Velocities*

The free-stream velocity affects the velocity entering the inlet of the propulsive wing, thus influencing the aerodynamic performance of the wing. Therefore, it is necessary to analyze the relationship between the aerodynamic characteristics of the propulsive wing and the free-stream velocity. The variation in the lift coefficient with free-stream velocity is depicted in Figure 19a. With the angle of attack and rotational speed held constant, the lift coefficient of the propulsive wing gradually decreases as the free-stream velocity increases, and the reduction in the lift coefficient becomes more significant with higher angles of attack. When the angle of attack and rotational speed remain constant, the mass flow rate entering the inlet remains consistent. As the free-stream velocity increases, the advance ratio of the propulsive wing decreases, leading to a reduction in the relative airflow acceleration on the upper surface, thereby causing a decrease in the lift coefficient. This signifies an increase in the relative velocity on the pressure side of the propulsive wing and a decrease in the acceleration effect of the airflow on the suction side. As the advance ratio further decreases, the suction capacity of the cross-flow fan becomes insufficient to control the boundary layer airflow, resulting in significant airflow separation on the upper surface of the propulsive wing, causing the lift coefficient to stabilize after decreasing to a certain value.

The variation in the drag coefficient with free-stream velocity is illustrated in Figure 19b. With the angle of attack and rotational speed held constant, the drag coefficient increases continuously as the free-stream velocity increases, leading to a decrease in the advance ratio. With further increases in the free-stream velocity, the advance ratio continues to decrease, indicating the insufficient suction capacity of the cross-flow fan, causing the propulsive wing to stall. Consequently, there is a significant decrease in the lift coefficient and a substantial increase in the drag coefficient.

The relationship between the torque coefficient and free-stream velocity is depicted in Figure 19c. With the angle of attack and rotational speed held constant, the torque coefficient shows a linear increasing trend with the increase in free-stream velocity. Moreover, at different angles of attack but the same free-stream velocity, the torque coefficients remain similar. As mentioned earlier, when the rotational speed is constant, the mass flow rate entering the cross-flow fan remains unchanged. However, with increasing free-stream velocity, the direction of the airflow entering the inlet changes, hindering the rotation of the blades near the inlet. This results in an increase in the torque coefficient. When the free-stream velocity is constant, the mass flow rate entering the cross-flow fan remains consistent at different angles of attack, indicating that the mass flow rate entering the cross-flow fan is independent of the angle of attack and dependent on the rotational speed [29].

In summary, embedding CFFs in the airfoil aims to control airflow during a high angle of attack flight, delaying separation over the airfoil surface. Compared to traditional wings, it enables higher lift coefficients and improved propulsion. Flow control parameters, including fan rotation speed, free-stream velocity, and angle of attack, can be selected based

on experimental findings. Fan rotational speed and free-stream velocity jointly determine the advance ratio. As the angle of attack increases, so does the likelihood of propulsive wing stall, necessitating a higher advance ratio. Consistency in the advance ratio is essential to maintain high lift coefficients. With an aircraft's free-stream velocity at 30 m/s, a fan speed of 9000 r/min is suitable for an eVTOL aircraft. This is relatively straightforward to achieve in engineering [30].
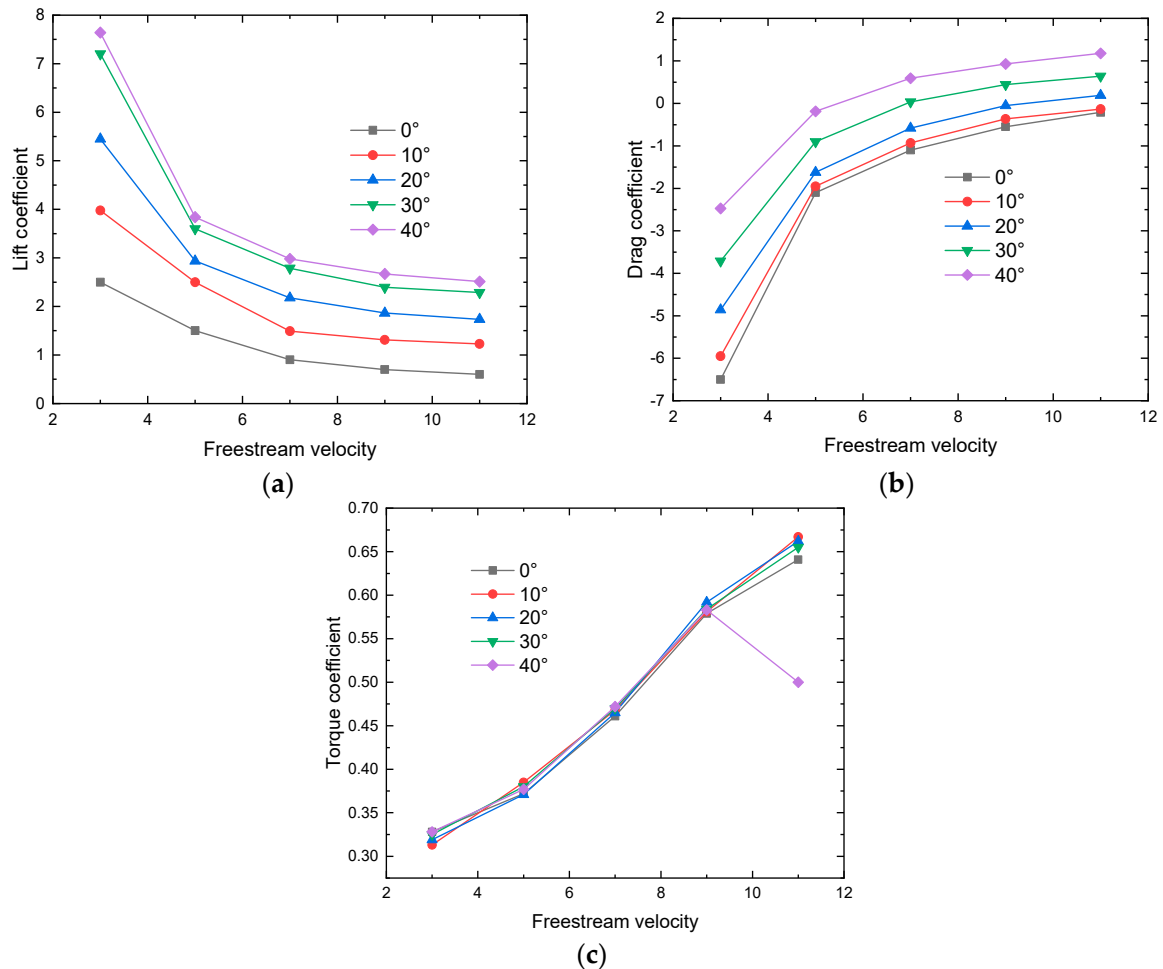
Figure 19. Aerodynamic performance of propulsive wing with different velocities ($\Omega = 3000$ r/min). (**a**) Lift coefficient by wind tunnel. (**b**) Drag coefficient by wind tunnel. (**c**) Torque coefficient by wind tunnel.

5. Conclusions

A novel design of an eVTOL aircraft with propulsive wings has been proposed in this paper. CFDs simulation methods and wind tunnel test methods applicable to propulsive wings were established. The aerodynamic lift-enhancing mechanism of the propulsive wing was analyzed, and the aerodynamic and flow field characteristics of the propulsive wing under different angles of attack, free-stream velocities, and rotational speeds were extensively studied. The following conclusions were drawn:

(1) Compared to traditional wings, the propulsive wing achieves remarkably high lift coefficients (exceeding 7.6 in experiments) and propulsion coefficients (exceeding 7.1 in experiments) at very high angles of attack (30°~40°) and low airspeeds. On the one hand, the CFF effectively controls the flow of the boundary layer, significantly delaying the airflow separation of the propulsive wing at high angles of attack; on the other hand, the rotation of the fan induces two eccentric vortices, generating vortex-induced lift and vortex-induced propulsion.

(2)   The aerodynamic characteristics of the propulsive wing are influenced by changes in the advance ratio and angle of attack. Typically, a higher advance ratio correlates with increased lift and propulsion coefficients, whereas a higher angle of attack is associated with higher lift and drag coefficients. The torque coefficient rises with the advance ratio, irrespective of the angle of attack and rotational speed.

(3)   The propulsive wing equipped with CFF circulation control capability is a novel high-lift device, offering a superior lift coefficient and reduced drag performance, making it a highly anticipated choice for eVTOL aircrafts. It demonstrates significant advantages in the low flight velocity range (0–30 m/s).

In the future, enhancing the aerodynamic efficiency of the propulsive wing will involve optimizing its configuration by modifying wing airfoil shape, cavity structure, and blade airfoil profile. This will enhance the flight efficiency and aerodynamic performance of eVTOL aircrafts.

6. Patents

This section is not mandatory but may be added if there are patents resulting from the work reported in this manuscript.

Nomenclature

UAM	Urban air mobility
eVTOL	Electrically driven vertical take-off and landing
CFF	Cross-flow fan
CFDs	Computational fluid dynamics
ESC	Electronic stability controller

Appendix A

(1)   The pressure variation along the arc-shaped groove of the propulsive wing

Without considering the influence of the fan position, the total pressure along the arc-shaped groove of the propulsive wing can be expressed as

$$H = \frac{p}{\rho g} + \frac{V^2}{2g} = \frac{p}{\rho g} + \frac{1}{2g}\left(V_r^2 + V_u^2\right) \tag{A1}$$

where p represents pressure, ρ denotes fluid density, g stands for gravitational acceleration, and V_r indicates the absolute velocity radial component.

According to the Navier–Stokes equation, the momentum equation in the *u* direction is

$$V_r \frac{\partial V_u}{\partial r} + \frac{V_u}{r} \frac{\partial V_u}{\partial \theta} + \frac{V_r V_u}{r} = -\frac{1}{\rho r} \frac{\partial p}{\partial \theta} \tag{A2}$$

In which *r* and *θ* are polar coordinates.

Eliminating the pressure *p*

$$V_r \left(\frac{1}{r} \frac{\partial V_r}{\partial \theta} - \frac{\partial V_\theta}{\partial r} - \frac{V_\theta}{r} \right) = \frac{g}{r} \frac{H}{\partial \theta} \tag{A3}$$

Given $\frac{1}{r} \frac{\partial V_r}{\partial \theta} - \frac{\partial V_\theta}{\partial r} - \frac{V_\theta}{r} = \gamma$, then

$$V_r \gamma = \frac{g}{r} \frac{\partial H}{\partial \theta} \tag{A4}$$

According to the Euler equation:

$$H = \frac{U V_u}{g} \tag{A5}$$

U is the linear velocity of the fan blades.

Therefore, the curl generated from the inlet to the outlet of the airflow is

$$V_r(\gamma_2 - \gamma_1) = \frac{g}{r} \frac{\partial (H_2 - H_1)}{\partial \theta} = \frac{U}{r} \frac{\partial (V_{u2} - V_{u1})}{\partial \theta} \tag{A6}$$

So

$$\gamma = \frac{\omega}{V_r} \frac{\partial}{\partial \theta} (V_{u2} - V_{u1}) \tag{A7}$$

ω is the angular velocity of the fan.

(2)   Variation in circulation around the blade

When the fan rotates, the circulation around the blade of the propulsive wing will change. According to Kelvin's theorem, vortices will form on both sides of the fan blade. As shown in Figure A1, the relative velocities on the pressure and suction sides of the fan blade tip are denoted as V_p and V_s, respectively. *γ* represents the vorticity intensity per unit length.
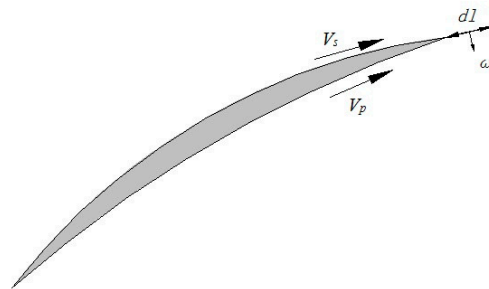
Figure A1. Flow diagram near the blade.

$$\gamma = V_s - V_p \tag{A8}$$

Assuming that the length of the vortex line generated within the time interval Δt is dl, then the increment of the circulation around the blade is

$$\Delta\Gamma = \gamma \mathrm{dl} = (V_s - V_p)\mathrm{dl} \tag{A9}$$

In a two-dimensional flow field, the region enclosed by any closed curve is divided into a series of elements by parallel coordinate lines. The velocity circulation of an elemental area is

$$
\begin{aligned}
d\Gamma = \int_{ABCDA} \vec{V} \cdot d\vec{S} &= \left(u + \frac{\partial u}{\partial x}\right)dx + \left(v + \frac{\partial v}{\partial y}dx + \frac{\partial v}{\partial y}\frac{dy}{2}\right)dy \\
&- \left(u + \frac{\partial u}{\partial y}dy + \frac{\partial u}{\partial x}\frac{dx}{2}\right)dx - \left(v + \frac{\partial v}{\partial y}\frac{dy}{2}\right)dy \\
&= \left(\frac{\partial v}{\partial x} - \frac{\partial u}{\partial y}\right)dxdy = 2\omega_z dxdy
\end{aligned}
\tag{A10}
$$

The circulation around the closed curve is

$$
\Gamma = \oint_L \vec{V} \cdot d\vec{s} = \oint_L (udx + vdy) = \int_S \left(\frac{\partial v}{\partial x} - \frac{\partial u}{\partial y}\right)dS = \int_S 2\omega_z dS
\tag{A11}
$$

From the above equation, it can be inferred that an increase in circulation will cause vortices to form at the wingtip of the blades during the operation of the propulsive wing, and the vorticity is related to the rotational speed.

According to the generalized Kutta–Joukowski theorem, the lift generated by any object in a flow field is

$$
L = \rho U_\infty \Gamma
\tag{A12}
$$

References

1. Pavel, M.D. Understanding the control characteristics of electric vertical take-off and landing (eVTOL) aircraft for urban air mobility. *Aerosp. Sci. Technol.* **2022**, *125*, 107143.1–107143.9. [CrossRef]
2. Sahoo, S.; Zhao, X.; Kyprianidis, K. A review of concepts, benefits, and challenges for future electrical propulsion-based aircraft. *Aerospace* **2020**, *7*, 44. [CrossRef]
3. Cole, J.A.; Rajauski, L.; Loughran, A.; Karpowicz, A.; Salinger, S. Configuration study of electric helicopters for urban air mobility. *Aerospace* **2021**, *8*, 54. [CrossRef]
4. Bacchini, A.; Cestino, E.; Van Magill, B.; Verstraete, D. Impact of lift propeller drag on the performance of eVTOL lift+cruise aircraft. *Aerosp. Sci. Technol.* **2021**, *109*, 106429. [CrossRef]
5. Brelje, B.J.; Martins, J.R.R.A. Electric, hybrid, and turboelectric fixed-wing aircraft: A review of concepts, models, and design approaches. *Prog. Aerosp. Sci.* **2019**, *104*, 1–19. [CrossRef]
6. Bacchini, A.; Cestino, E. Electric VTOL configurations comparison. *Aerospace* **2019**, *6*, 26. [CrossRef]
7. Stokkermans, T.; Usai, D.; Sinnige, T.; Veldhuis, L.L.M. Aerodynamic Interaction Effects Between Propellers in Typical eVTOL Vehicle Configurations. *J. Aircr.* **2021**, *58*, 815–833. [CrossRef]
8. Ma, T.; Wang, X.; Qiao, N.; Zhang, Z.; Fu, J.; Bao, M. A Conceptual Design and Optimization Approach for Distributed Electric Propulsion eVTOL Aircraft Based on Ducted-Fan Wing Unit. *Aerospace* **2022**, *9*, 690. [CrossRef]
9. Pelz, P.; Liese, P.; Meck, M. Sustainable aircraft design—A review on optimization methods for electric propulsion with derived optimal number of propulsors. *Prog. Aerosp. Sci.* **2021**, *123*, 100714.1–100714.28. [CrossRef]
10. Menegozzo, L.; Benini, E. Boundary Layer Ingestion Propulsion: A Review on Numerical Modelling. *J. Eng. Gas Turbines Power* **2020**, *142*, 120801–120815. [CrossRef]
11. Kim, H.; Liou, M. Flow simulation and optimal shape design of N3-X hybrid wing body configuration using a body force method. *Aerosp. Sci. Technol.* **2017**, *71*, 661–674. [CrossRef]
12. Dang, T.; Bushnell, P. Aerodynamics of Cross-flow Fans and their Application to Aircraft Propulsion and Flow Control. *Prog. Aerosp. Sci.* **2009**, *45*, 1–29. [CrossRef]
13. Guo, J.; Zhou, Z. Multi-Objective Design of a Distributed Ducted Fan System. *Aerospace* **2022**, *9*, 165. [CrossRef]
14. Kummer, J.; Dang, T. High-Lift Propulsive Airfoil with Integrated Cross-flow Fan. *J. Aircr.* **2006**, *43*, 1059–1068. [CrossRef]
15. Waterman, T. Development of Improved Design and 3D Printing Manufacture of Cross-Flow Fan Rotor. Ph.D. Dissertation, Naval Postgraduate School, Monterey, CA, USA, 2016.
16. Perry, A.; Ansell, P.; Kerho, M.; Ananda, G. Design, analysis, and evaluation of a propulsive wing concept. In Proceedings of the 34th AIAA Applied Aerodynamics Conference, Washington, DC, USA, 13–17 June 2016. [CrossRef]
17. Walter, A.; McKay, M.; Niemiec, R.; Gandhi, F.; Berger, T. Hover dynamics and flight control of a UAM-scale quadcopter with hybrid rpm and collective pitch control. *J. Am. Helicopter Soc.* **2023**, *68*, 143–160. [CrossRef]
18. Wang, J.; Chen, R.; Lu, J. Experimental and Numerical Studies on the Effect of Airflow Separation Suppression on Aerodynamic Performance of a Ducted Coaxial Propeller in Hovering. *Aerospace* **2023**, *10*, 11. [CrossRef]
19. Deng, J.; Sun, L.; Shao, X. Wake dynamics of low-Reynolds-number flow around a two-dimensional airfoil. *Phys. Fluids* **2019**, *31*, 024102. [CrossRef]
20. Lu, J.; Lu, Y.; Wang, J. Numerical investigation of the quasi-vortex-ring state of the propulsive wing in vertical descent. *Aerosp. Sci. Technol.* **2023**, *132*, 108075. [CrossRef]

21. Anoop, S.; Velamati, R.K.; Oruganti, V.R.M. Aerodynamic characteristics of an aerostat under unsteady wind gust conditions. *Aerosp. Sci. Technol.* **2021**, *113*, 106684. [CrossRef]
22. Zheng, Y.; Qu, Q.; Liu, P.; Wen, X.; Zhang, Z. Numerical analysis of the porpoising motion of a blended wing body aircraft during ditching. *Aerosp. Sci. Technol.* **2021**, *119*, 107131. [CrossRef]
23. Gharali, K.; Johnson, D.A. Numerical modeling of an S809 airfoil under dynamic stall, erosion and high reduced frequencies. *Appl. Energy* **2012**, *93*, 45–52. [CrossRef]
24. Wang, J.; Chen, R.; Yu, Z.; Lu, J. Ground test and numerical investigation on aerodynamic performance of a quad tilt-rotor aircraft in ground and water effects. *Ocean Eng.* **2023**, *289*, 116169. [CrossRef]
25. Tugnoli, M.; Montagnani, D.; Syal, M.; Droandi, G.; Zanotti, A. Mid-fidelity approach to aerodynamic simulations of unconventional VTOL aircraft configurations. *Aerosp. Sci. Technol.* **2021**, *115*, 106804. [CrossRef]
26. Faure, T.M.; Hétru, L.; Montagnier, O. Aerodynamic features of a two-airfoil arrangement. *Exp. Fluids* **2017**, *58*, 146. [CrossRef]
27. Lagopoulos, N.S.; Weymouth, G.D.; Ganapathisubramani, B. Deflected wake interaction of tandem flapping foils. *J. Fluid Mech.* **2020**, *903*, A9. [CrossRef]
28. Boschitsch, B.M.; Dewey, P.A.; Smits, A.J. Propulsive performance of unsteady tandem hydrofoils in an in-line configuration. *Phys. Fluids* **2014**, *26*, 051901. [CrossRef]
29. Askari, S.; Shojaeefard, M. Experimental and numerical study of an airfoil in combination with a cross flow fan. *Proc. Inst. Mech. Engineers. Part G J. Aerosp. Eng.* **2013**, *227*, 1173–1187. [CrossRef]
30. Kasem, A.; Gamal, A.; Hany, A.; Gaballa, H.; Ahmed, K.; Romany, M.; Abdelkawy, M.; Abdelrahman, M.M. Design and implementation of an unmanned aerial vehicle with self-propulsive wing. *Adv. Mech. Eng.* **2019**, *11*, 1–10. [CrossRef]